Microscopic model approach to (n,xn) pre-equilibrium reactions for medium-energy neutrons

M. Dupuis* and T. Kawano
Theoretical Division, Los Alamos National Laboratory, Los Alamos, New Mexico 87545, USA

J.-P. Delaroche and E. Bauge
CEA, DAM, DIF, F-91297 Arpajon, France

(Received 15 October 2010; revised manuscript received 19 November 2010; published 7 January 2011)

We report on microscopic model calculations of the first step of direct pre-equilibrium (n,xn) emission in neutron interaction with ^{90}Zr and ^{208}Pb below 20 MeV. Our model is based on both an accurate description of the target excited states, provided by the self-consistent random-phase approximation (RPA) method implemented with the Gogny D1S force, and well-established in-medium two-body forces to represent the residual nucleon-nucleon interaction for the inelastic processes. Two goals have been achieved: The present microscopic approach provides a unified description of collective state excitations and the pre-equilibrium one-step process, and our reaction model reproduces the available data fairly well, without any parameter adjustment.

DOI: 10.1103/PhysRevC.83.014602 PACS number(s): 24.10.Eq, 21.60.Jz, 24.50.+g, 25.40.Fq

I. INTRODUCTION

Over the past two decades, quantum-mechanical pre-equilibrium models extensively used to analyze nucleon-induced reactions have reached maturity. Two main pre-equilibrium mechanisms are usually considered. The first, known as the multistep direct (MSD) process, assumes that the projectile collides one or several times with the target nucleus but at least one nucleon remains in the continuum. In the second, the multistep compound (MSC) process, the projectile is first absorbed by the nucleus and re-emitted rather rapidly, before the composite system reaches the statistic equilibrium state of a compound nucleus. The original MSC and MSD models developed by Feshbach, Kerman, and Koonin (FKK) [1] have been extended to account for reaction mechanisms such as transfer of flux between the MSD and MSC chains [2], multiple-particle emission during the MSD process [3], and interference effects in the second step of the MSD [4], which were not considered in the early days of pre-equilibrium reaction modeling.

It was shown [2] that the MSD mechanism dominates the pre-equilibrium emission for nuclear-induced reaction at incident neutron energy as low as 14 MeV [2], and that below ∼25 MeV, second and higher order direct processes are weak. A MSD calculation is thus reduced to a one-step direct process, which is equivalent to treating excitation of the target nucleus after one interaction has taken place with the projectile. This process may be modeled in the distorted-wave Born approximation (DWBA) for inelastic transitions to the continuum. Although the one-step process is relatively simple compared to other pre-equilibrium mechanisms that have been studied so far, its modeling still requires several phenomenological ingredients, such as state densities and optical model potentials. So far, its implementation also systematically uses a very simple representation of the residual two-body interaction, the parameters of which are directly adjusted to fit experimental spectra. Koning and Chadwick [5] reduced the role of phenomenology in MSD calculations, as these authors computed cross sections for each particle-hole (p-h) state built from a pertinent Nilsson scheme, so their model did not require phenomenological state densities.

Moreover, in medium-energy nucleon-induced reaction analyses typically covering the 10- to 200-MeV range, the so-called direct (collective) reactions are usually distinguished from the pre-equilibrium MSD process [5,6]. We note that this distinction is also made in studies based on the exciton pre-equilibrium model [7]. The direct reactions correspond to the excitation of sharp states at low excitation energies, such as low-lying collective states, or to giant resonances which are embedded in the continuum. The MSD pre-equilibrium model so far relies on statistical assumptions, such as the leading particle statistics or the residual system statistics [8], and uses incoherent p-h excitations to account for target states at excitation energy higher than a few MeV. Besides the inconsistency in the modeling, the distinction between direct reactions with collective excitations and the MSD process applied with statistical assumptions leads to a double counting between coherent p-h excitations (i.e., collective modes) and incoherent p-h excitations, which has been partially cured using phenomenological means [5,9]. Direct collective contributions are usually calculated within a phenomenological collective model that takes as input the multipole deformation parameters β_L extracted from high-precision proton-inelastic-scattering studies [6]. However, while reliable information about collective low-lying states are available, the collectivity in nuclear spectra above the few low-lying collective states is not experimentally well known in general. Consequently, the contribution of this portion of collective spectra is either ignored [5] or included using the assumption that the β_L values for collective states are determined from an assumed fraction of the energy-weighted sum rule (EWSR) [7,9]. As the distribution over the excitation energy of these strengths is not always well established, even for giant resonances, calculated cross sections for collective states above the low-lying excitations strongly depend on the prescription adopted for distributing the β_L strengths over excitation energy.

*Permanent address: CEA, DAM, DIF, F-91297 Arpajon, France; marc.dupuis@cea.fr

In the quantum-mechanical pre-equilibrium formalism of Tamura, Udagawa, and Lenske (TUL) [10], the collective and noncollective excitations are accounted for by transition-strength functions provided by the random-phase approximation (RPA). The one-step cross section in TUL, although based on a microscopic description of the nuclear excitation, is factorized into the RPA strength and inelastic-scattering DWBA cross section averaged over the different p-h components, in which the detailed connection between the scattering and residual states inevitably gets lost.

In this study we propose quantum-mechanical calculations of the one-step direct contribution to the pre-equilibrium process that use reliable residual two-body interactions as well as a microscopic description of target states. The self-consistent RPA (SCRPA) method implemented with the Gogny D1S interaction [11] is used to provide our description of the target excitations. This allows us to calculate simultaneously the direct and the one-step contributions in a unified way. Moreover, our model does not contain any adjustable parameter so that the results of calculations can directly be compared with experimental data.

In Sec. II we briefly review the quantum-mechanical formulation of the one-step direct process. We detail the different ingredients that are used in our calculations, namely, the structure of target state excitations, two-body residual interactions, and distorted waves. In Sec. III we compare our model predictions with experimental data for (n,xn) double-differential cross sections calculated for 10- to 20-MeV neutron-induced reactions on the spherical ^{90}Zr and ^{208}Pb target nuclei. Sensitivity of the calculated cross sections to the choice of the residual two-body interaction and to the collectivity content of target state excitations is examined. Decomposition of cross sections over the spin and parity of target excitations is also detailed, and we discuss figures of merit of the present model. Finally, a conclusion and outlook are provided in Sec. IV.

II. METHOD

In this section we first provide a brief account of the well-known quantum-mechanical pre-equilibrium model of the one-step emission process. Next we provide a detailed description of RPA excitations and residual interactions used in the modeling of the ^{90}Zr(n,n') and ^{208}Pb(n,n') reactions to be studied later in Sec. III.

A. Reaction theory

The quantum pre-equilibrium model for the MSD process is based on the Born series of the probability amplitude $T_{F\leftarrow 0}$, corresponding to the transition between an initial state made up of an incident nucleon of momentum $\mathbf{k}_i$ and target in its ground state $|0\rangle$, and a final state made up of an outgoing nucleon of momentum $\mathbf{k}_f$ and target in excited state $|F\rangle$ [1], namely,

$$T_{F\leftarrow 0} = \langle \chi^{(-)}(\mathbf{k}_f), F|V_{\rm res}\sum_{n=1}^{\infty}\left(\frac{1}{PHP-E+i\epsilon}V_{\rm res}\right)^{n-1} \times |\chi^{(+)}(\mathbf{k}_i),0\rangle = \sum_{n=1}^{\infty} T^{(n)}_{F\leftarrow 0}, \quad (1)$$

where $V_{\rm res}$ is the residual interaction responsible for the inelastic process, E is the total energy of the system, $H = H_A + H_1$ is the unperturbed Hamiltonian (i.e., target Hamiltonian plus projectile Hamiltonian), P is the projector on the space spanned by scattering states, and $\chi^{(+/-)}(\mathbf{k}_{i/f})$ is the distorted wave in the entrance or exit channel. The nth term is associated with the n-step component of the pre-equilibrium MSD process.

The MSD double-differential cross section reads

$$\frac{d^2\sigma(\mathbf{k}_i,\mathbf{k}_f)}{d\Omega_f dE_{k_f}} = \frac{1}{2e}\int_{E_{k_f}-e}^{E_{k_f}+e} dE_k \frac{\mu^2}{(2\pi\hbar^2)^2}\frac{k}{k_i} \times \sum_F |T_{F\leftarrow 0}|^2\,\delta(E_{k_i}-E_k-E_F), \quad (2)$$

where E_{k_i/k_f} is the energy of the nucleon in the entrance or exit channel and $E_F = \langle F|H_A|F\rangle - \langle 0|H_A|0\rangle$ is the target excitation energy. The sum over F includes all target excited states. In Eq. (2) the average over the outgoing nucleon energy E_{k_f} within a $2e$ width accounts for both the energy bins in measurements and the energy resolution of the experimental devices. This expression should also be averaged over the incoming nucleon energy if the beam is only quasi-mono-energetic, which often happens in neutron-scattering experiments at medium energies.

The lowest order of the MSD mechanism corresponds to the one-step process. In that case, the transition amplitude $T_{F\leftarrow 0}$ reduces to the first term of Eq. (1), namely,

$$T^{(1)}_{F\leftarrow 0} = \langle \chi^{(-)}(\mathbf{k}_f), NJM\Pi|V_{\rm res}|\chi^{(+)}(\mathbf{k}_i),0\rangle, \quad (3)$$

and the one-step double-differential cross section reads

$$\frac{d^2\sigma^{(1)}(\mathbf{k}_i,\mathbf{k}_f)}{d\Omega_f dE_{k_f}} = \frac{1}{2e}\int_{E_{k_f}-e}^{E_{k_f}+e} dE_k \frac{\mu^2}{(2\pi\hbar^2)^2}\frac{k}{k_i} \times \sum_N |\langle \chi^{(-)}(\mathbf{k}_f), NJM\Pi|V_{\rm res}|\chi^{(+)}(\mathbf{k}_i),0\rangle|^2 \times \delta(E_{k_i}-E_k-E_N). \quad (4)$$

The state $|F\rangle = |NJM\Pi\rangle$ represents an excitation of total angular momentum J, projection M, parity Π, and excitation energy E_N. The ground state $|0\rangle$ has zero angular momentum and positive parity, because we only consider spherical even-even nuclei in this study. In the case of a nonzero target, the angular momentum coupling between the initial and final states can be dealt with. However, the effect of the target spin might not be that large when the final-state-configuration-phase space is large enough.

We introduce the one-body density-transition-matrix elements (OBDTMEs) associated with the transition between the target ground state $|0\rangle$ and one excited state $|NJM\Pi\rangle$. They read

$$\rho^{0,F}_{\beta,\alpha} = \langle NJM\Pi|a^{\dagger}_{\alpha}\times a_{\beta}|0\rangle, \quad (5)$$

where the single-particle (s.p.) operators $a^{\dagger}_{\alpha}$ and a_{β} correspond to the creation and annihilation of a particle in a s.p. state belonging to the basis $\{\alpha\}$, respectively. This s.p. basis can

be defined as the set of the target nucleus Hartree-Fock (HF) mean-field solutions. The transition amplitude, Eq. (3), is expressed as a combination of OBDTMEs and two-body matrix elements of the residual interaction $V_{\rm res}$, namely,

$$T^{(1)}_{F\leftarrow 0} = \sum_{\alpha,\beta} \langle \chi^{(-)}(\mathbf{k}_f), \alpha | V_{\rm res} | \chi^{(+)}(\mathbf{k}_i), \beta \rangle_A \;\; \rho^{0,F}_{\beta,\alpha}, \tag{6}$$

where the A symbol attached to matrix elements indicates antisymmetrization. More details about this derivation can be found in [12]. The OBDTMEs, Eq. (5), are the spectroscopic information that must be known prior to calculating all the one-step process components.

B. Target states in SCRPA

The structure properties for both ground and excited states are described by the SCRPA method [13] implemented with the Gogny D1S force [11]. For ^{208}Pb, this nuclear structure model, hereafter labeled SCRPA+D1S, provides a good description of the properties for low-lying collective states and giant multipole resonances [14,15], for many other states that have weaker but non-negligible collectivity [16], and for high-spin and non-natural parity states [16,17]. Spectroscopic properties for ^{90}Zr are less accurately described than those for ^{208}Pb by the present model as (i) the weak pairing content of the $Z = 40$ proton subshell is neglected here, and (ii) two-particle–two-hole excitations required to form the yrast 2^+ and 4^+ states are outside the RPA model space [18]. Nevertheless, for ^{90}Zr, the SCRPA+D1S approach accurately reproduces the properties of most low-lying collective states as well as giant resonances, both of which are shown to be of prime importance in the reaction model analyses presented in the next section.

All details on the SCRPA+D1S method can be found in [13,14,17], so here we simply point out that in the RPA approximation, an excited state $|NJM\Pi\rangle$ [Eqs. (3)–(5)] reads

$$|NJM\Pi\rangle = \Theta^{\dagger}_{NJM\Pi}|\tilde{0}\rangle, \tag{7}$$

where the ket $|\tilde{0}\rangle$ represents the RPA-correlated ground state. The operator $\Theta^{\dagger}$ stands for the creation of a boson and reads

$$\Theta^{+}_{NJM\Pi} = \sum_{ph} X^{NJ\Pi}_{ph} A^{\dagger}_{JM\Pi}(p\tilde{h}) - Y^{NJ\Pi}_{ph} A_{J\bar{M}\Pi}(p\tilde{h}), \tag{8}$$

where $A^{\dagger}_{JM\Pi}$ and $A_{J\bar{M}\Pi}$ are the angular momentum coupled creation and annihilation operators of a p-h pair, respectively, defined in Ref. [12]. The single-particle states are defined with respect to the HF mean field. Remember that in Eq. (8) the sum runs separately over proton and neutron p-h states. The transition operator [Eq. (8)] contains both isoscalar, $T = 0$, and isovector, $T = 1$, components, where T is the isospin. The total angular momentum J corresponds to the coupling of the orbital angular momentum L to the intrinsic spin S.

The amplitudes $X^{NJ\Pi}_{ph}$ and $Y^{NJ\Pi}_{ph}$ are related to OBDTMEs [Eq. (5)] as follows:

$$\begin{aligned} X^{NJ\Pi}_{ph} &= \langle NJM\Pi | A^{\dagger}_{JM\Pi}(p\tilde{h}) | \tilde{0} \rangle, \\ Y^{NJ\Pi}_{ph} &= \langle NJM\Pi | A^{\dagger}_{JM\Pi}(\tilde{h}p) | \tilde{0} \rangle. \end{aligned} \tag{9}$$

The double-differential cross section [Eq. (4)] is obtained by calculating the transition amplitudes [Eq. (6)] for all possible transitions specified by the RPA amplitudes [Eq. (9)].

Although the SCRPA+D1S method provides a good overall description of the spectroscopic properties of the two nuclei under study, couplings to two or more p-h states and to continuum states are neglected. These couplings impact as a redistribution of strengths and shift positions of the RPA eigenstates [19,20]. To first-order approximation, couplings to states that are outside the RPA model space can be handled by assigning a finite width Γ_N and an energy shift Δ_N to each RPA state. A microscopic calculation of these corrections is outside the scope of the present study. We use a phenomenological estimate for the damping plus the escape width $\Gamma_N = 0.026 E_N^{1.9}$ MeV [21], to which we add a width stemming from the energy resolution of the neutron beam. This last term is represented using a Gaussian distribution of width $\Gamma \simeq 0.5$–1.3 MeV, depending upon incident energy, which corresponds to the spreading of the elastic peaks displayed in the neutron emission spectra analyzed in Sec. III.

The energy shift Δ_N is chosen to approximately compensate for differences between SCRPA+D1S and experimental energies of well-known excitations, since the predicted E_N values tend to be higher. Experimental excitation energies of the first 3^-, 5^-, 2^+, 4^+, 6^+, 8^+, and 10^+ excitations for ^{208}Pb [22], the first 3^- and 5^- excitations in ^{90}Zr [23], and systematic energies of giant resonances [21] for both nuclei are used as references to calculate the Δ_N values. For giant resonances, we use the reference excitation energies $E_x \simeq \alpha A^{-1/3}$, with $\alpha = 31$ MeV for the low-energy octupole resonances (LEOR), $\alpha = 80$ MeV for the isovector giant dipole resonance (IVGDR), and $\alpha = 80$ and 63 MeV for the isoscalar giant monopole and quadrupole resonances (ISGMR and ISGQR) [21], respectively. The Δ_N corrections for all states that are not directly anchored to an experimental value, or to a value from systematics, have been determined using a simple interpolation. For ^{90}Zr, the RPA energies are shifted by a Δ_N value smaller than 200 keV for low-lying states and by Δ_N values in the range 0.7–1.5 MeV for giant resonances. For ^{208}Pb, the Δ_N values reach approximatively 1 MeV for low-lying states and 1–2 MeV for giant resonances.

For our applications, the SCRPA+D1S equations were solved by expanding solutions on a harmonic oscillator basis, including 14 major shells and assuming no space truncation. Note that all RPA excited states with spin J up to $J = 14$ ($\hbar$ units) with natural [$\Pi = (-)^J$, i.e., $J = L$] and non-natural [$\Pi = (-)^{J+1}$, i.e., $J = L \pm 1$] parities are considered. Transition amplitudes [Eq. (6)] are calculated with the computer code DWBA98 [24]. The full expression of the transition amplitudes [Eq. (6)], which includes angular momentum coupling details and different components of the two-body interaction $V_{\rm res}$ for direct and exchange terms, can be found in Refs. [24,25]. Note that the present one-step direct model, which uses the SCRPA+D1S nuclear-structure approach, has been established and employed in the previous microscopic pre-equilibrium study of Ref. [26].

C. Transition probabilities

We perform an analysis of reduced transition probabilities for the excitation of natural parity states that characterizes the collectivity content of the two targets' spectra. This is useful in the later interpretation of the calculated one-step cross section [Eq. (4)].

For any natural parity $J^\Pi \to 0^+$ transition, the reduced electric transition probability is defined as

$$B(EJ, 0^+ \leftarrow J^\Pi) = \sum_M \left| \langle NJM\Pi | r^J Y^J_M | 0 \rangle \right|^2, \quad (10)$$

where $r^J Y^J_M$ is the transition operator. The $B(EJ)$ values [Eq. (10)] are calculated with the RPA wave functions [Eq. (7)] or with p-h excitations of the uncorrelated HF mean field, defined as

$$|NJM\Pi\rangle_{ph} = A^\dagger_{JM\Pi}(p\tilde{h})|0\rangle, \quad |0\rangle = |\mathrm{HF}\rangle. \quad (11)$$

Remember that collective states generate much stronger transition densities than do those for single p-h states. The comparison between p-h and RPA transition probabilities provides a measure of the collectivity content of the nuclei spectra.

By performing this comparison for all transitions with a total angular momentum transfer in the range $J = 0$–14, it is shown that the nuclear spectrum contains non-negligible collectivity for natural parity transitions up to $J = 6$ in ^{90}Zr and up to $J = 8$ in ^{208}Pb. In each nucleus, the RPA and p-h strengths become very similar for higher J values. To be more specific, we focus on the 3^- and 5^- excitations, which are the most relevant to this study. The E3 and E5 strength functions [Eq. (10)] are displayed in Figs. 1 and 2 for ^{90}Zr and ^{208}Pb, respectively. The excitation energies E_x in the plots correspond to the corrected energies $E_N - \Delta_N$ defined in Sec. II B.

For ^{90}Zr, the RPA E3 strength in Fig. 1(b) has significant contributions below $E_x = 9$ MeV, and it mainly contains a very collective low-lying state at $E_x = 2.7$ MeV, as well as the LEOR centered at $E_x = 6.9$ MeV. The RPA E5 strength in Fig. 1(d) is mainly concentrated in two states: a low-lying state located at $E_x = 2.2$ MeV and a state that displays strong collectivity located at $E_x = 9.8$ MeV. The E3 and E5 p-h strengths seen in Figs. 1(a) and 1(b), respectively, are significantly lower that those for RPA and mainly contribute above $E_x \simeq 8$ MeV. These differences characterize the collective content of the spectrum of present interest.

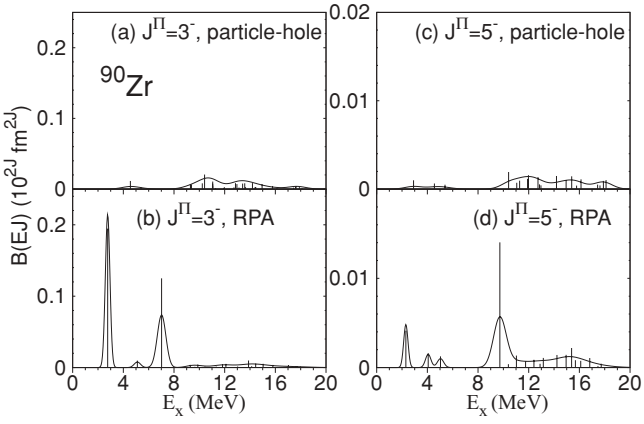

FIG. 1. Strength functions [Eq. (10)] for E3 and E5 excitations in ^{90}Zr as described with one p-h or RPA operator. Vertical bars are for the strengths at discrete energies E_x. Full curves are obtained from folding the strength functions with a Gaussian distribution (curves are scaled by a factor of 0.5).

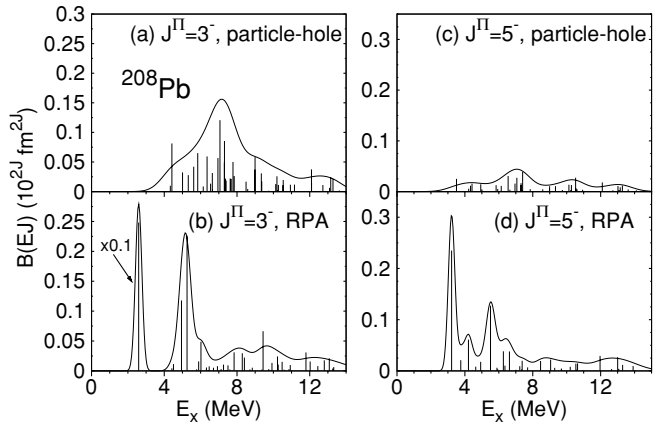

FIG. 2. Same as Fig. 1 for ^{208}Pb.

In ^{208}Pb, the RPA E3 strength in Fig. 2(b) is mostly concentrated below $E_x = 7$ MeV, with a very collective low-lying state at $E_x = 2.6$ MeV and the LEOR centered at $E_x = 5.2$ MeV. The RPA E5 strength in Fig. 2(d) displays large collectivity below $E_x = 7$ MeV. The p-h strengths in Figs. 2(a) and 2(b) are significantly smaller than those for RPA solutions and are concentrated at higher energy.

D. Residual interaction for inelastic transitions

We now provide some details about the effective two-body interactions, V_{res} in Eq. (6), that are used in our one-step direct calculations. In all previous quantum pre-equilibrium calculations this residual interaction was represented by a simple central interaction with a Yukawa form factor (see Ref. [5] as an example) for which the strength was adjusted to reproduce experimental cross sections. As our goal is to perform calculations that can be directly compared to experimental data without any adjustment being made, we consider reliable interactions for which the parameters are fixed and not adjusted to match nucleon-scattering experimental data.

However, for the reactions under study here, this requirement can be only partially fulfilled. While at higher incident energy (above approximately 50 MeV) the Melbourne g matrix [27], used as an effective interaction in microscopic folding model calculation, provides very accurate predictions for proton elastic [12,27] and inelastic scattering [16,28], a good representation of the effective interaction to be used in a direct reaction model at lower energy is still lacking and a more complicated reaction mechanism should be considered as well [12]. Nonetheless, we consider that g matrices could still provide a reasonable description of the residual interaction, but we do not expect the same degree of accuracy below ~50 MeV as that reached in proton-scattering studies at higher incident energy.

Accordingly, we use the density-dependent extensions CDM3Y*n* [29] (where *n* ranges from 1 to 6) of the effective interaction M3Y [30] based on the g-matrix elements of the Paris NN potentials. For comparison, we also consider the original M3Y interaction [30]. Other density-dependent extensions of M3Y, such as the DDM3Y and BDM3Y interactions [29], have also been tested in our one-step MSD calculations, but as these lead to predictions very close to those obtained with the CDM3Y*n* parametrizations, they are not discussed here. These interactions all contain central (in the four spin-isospin $S = 0, 1$ and $T = 0, 1$ channels), spin-orbit ($T = 0, 1$), and tensor ($T = 0, 1$) components [30]. The density dependence originally was introduced in the central term of the M3Y force to ensure the reproduction of saturation properties of nuclear matter. An additional energy dependence was also introduced to simulate the energy dependence of the nucleon optical potential [31].

Finally, we indicate that the distorted waves entering the transition amplitudes [Eq. (3)] have been obtained in both incoming and outgoing channels using the phenomenological Koning-Delaroche optical potential [32].

III. RESULTS AND DISCUSSION

In this section we present the results of our (n, n') one-step calculations for the scattering of 14- and 18-MeV neutrons from the ^{90}Zr and ^{208}Pb targets. We first investigate the effect of the residual two-body interaction on the calculated cross sections. Next we compare our predictions with (*n*,*xn*) experimental data and emphasize how a precise description of the excited states impacts predictions. Finally, we explain how our calculation avoids some of the deficiencies met in previous analyses, and we discuss the approximations we made to assess uncertainties in the present model predictions.

A. Sensitivity to effective interaction

As explained in the previous section, the effective two-body residual interaction $V_{\rm res}$ [Eq. (6)] to be used at relatively low energies should be considered carefully before making any comparison with the data. We compare the calculated cross sections [Eq. (4)] using the M3Y, CDM3Y1, and CDM3Y6 effective interactions. These three sets of calculations are performed with the RPA excitation [Eq. (7)]. The results for the 18-MeV neutron scattering from ^{90}Zr are displayed in Fig. 3(a) for the angle-integrated double-differential cross section in Eq. (4) for outgoing energies $E_{\rm out}$ in the range 0–18 MeV (the contribution from elastic scattering is not included) and in Fig. 3(b) for the angular distribution of emitted neutrons at the outgoing energy $E_{\rm out} = 11$ MeV. In both figures the two cross sections calculated with CDM3Y1 (dashed curves) and CDM3Y6 (dotted curves) are almost identical in shape, and their magnitudes differ by approximately 5%. Results based on CDM3Y*n*, with *n* ranging from 2 to 5, are between those for CDM3Y6 and CDM3Y1 so they are not displayed. We notice that results obtained with the two CDM3Y interactions (dotted and dashed curves) are up to 30% larger than those obtained with M3Y (full curves). This difference stems from a

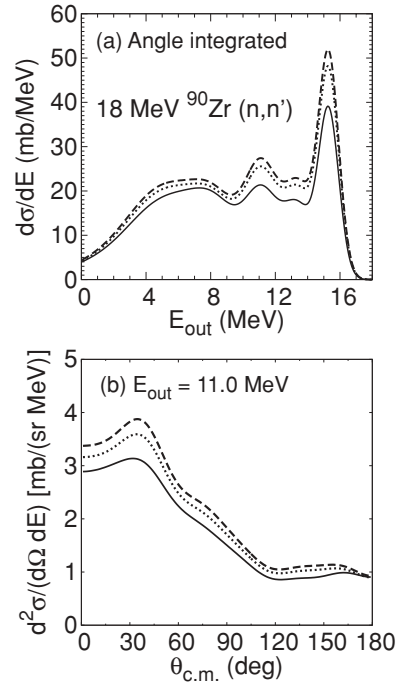

FIG. 3. (*n*,*xn*) spectra and angular distributions for 18-MeV neutrons incident on ^{90}Zr. One-step cross sections calculated with the M3Y (full curves), CDM3Y1 (dashed curves), and CDM3Y6 (dotted curves) interactions: (a) angle-integrated neutron emission spectra and (b) angular distributions at $E_{\rm out} = 11$ MeV.

combination of two effects. The energy dependence included in CDM3Y*n* interactions leads to a reduction in the cross sections by 3%–7%, but the explicit density dependence greatly increases the cross sections. This enhancement is understood as follows: We know that a density dependence in a nuclear interaction usually acts as a repulsive interaction. However, the original M3Y interaction [30] corresponds to a *g*-matrix calculation that is an average over a range of densities [33]. Since low-energy projectiles mainly probe the surface, low-density part of the target, repulsion effects are most likely overestimated in the present calculation performed with M3Y. The explicit density dependence in CDM3Y *n* corrects for this effect.

The comparison between the two-body interactions used in our calculations provides us with estimates for uncertainty in predictions. From the present study, this uncertainty can be represented by a global normalization factor of approximately 30%. While we do not expect any greater variations related to the choice between different effective interactions, a more systematic study should be performed to evaluate this uncertainty with better precision than presently achieved. Using a microscopic residual interaction that is fixed for all the reactions under study represents significant progress nonetheless. Indeed, previous MSD calculations used simple central phenomenological interactions with parameters directly adjusted to fit the experimental distributions. The strengths of these interactions thus displayed strong variations between different studies, as they may depend on (i) projectile and target, (ii) adopted prescriptions for the phenomenological

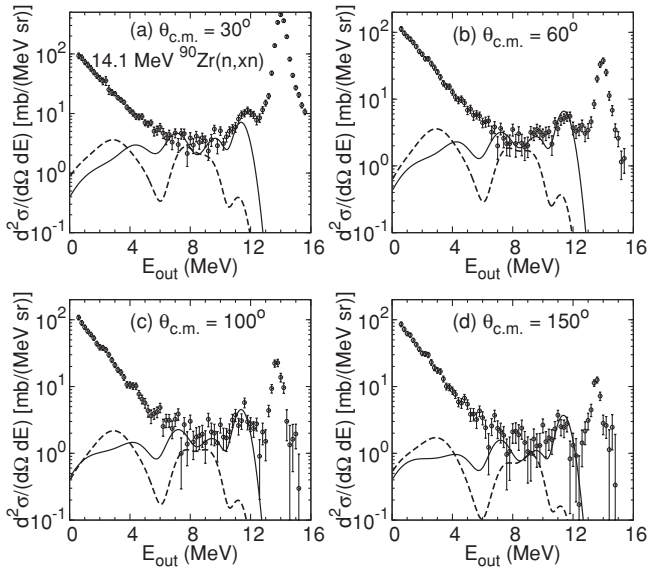

FIG. 4. (n,xn) spectra for 14.1-MeV neutrons incident on ^{90}Zr. Calculated one-step contributions to the neutron emission spectra compared to experimental (n,xn) data [34] (open circles). Full and dashed curves are for cross sections calculated using the RPA and p-h excitations, respectively. Outgoing angles are indicated on panels (a), (b), (c), and (d).

level densities and optical potential, as well as (iii) relative contributions of other reaction mechanisms (i.e., two-step direct, MSC, direct collective reaction, and evaporation processes) to (n,xn) emission.

B. Comparison to experimental data

Next we compare the calculated one-step double-differential cross sections [Eq. (4)] to experimental (n,xn) data for ^{90}Zr and ^{208}Pb in Figs. 4–9. All calculations (full curves) were performed with the CDM3Y3 interaction and

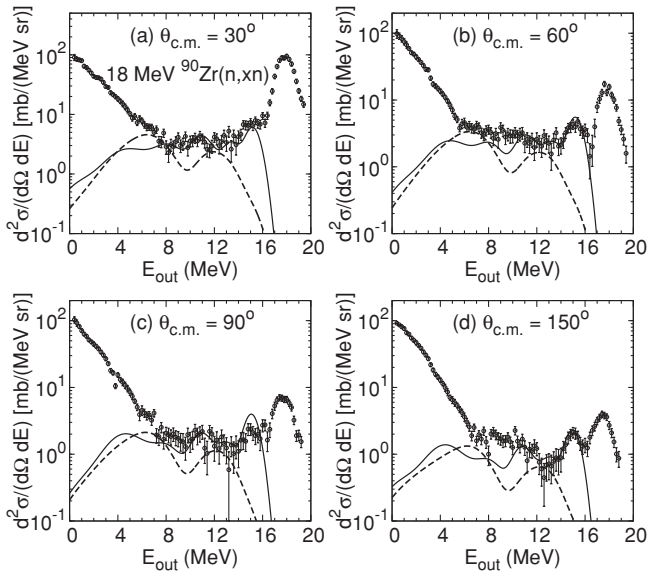

FIG. 5. Same as Fig. 4 for 18-MeV incident energy.

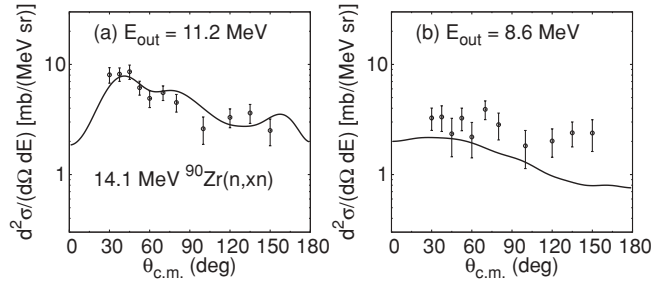

FIG. 6. (n,xn) angular distributions for 14.1-MeV neutrons incident on ^{90}Zr. Cross sections calculated with the CDM3Y3 interaction (full curves) are compared to experimental data [34] (open circles). The neutron outgoing energies $E_{\rm out}$ are indicated on panels (a) and (b).

the RPA states of Eq. (7), including those with natural and non-natural parities. Cross sections are displayed in two representations, that is, as a function of the emission energy $E_{\rm out}$ at selected outgoing angles $\theta_{\rm c.m.}$ (spectra), and as a function of $\theta_{\rm c.m.}$ at selected $E_{\rm out}$ values (angular distributions). Note that neither calculated elastic scattering nor nondirect interaction contributions to the neutron emission spectra are displayed in Figs. 4–9.

1. ^{90}Zr target

Comparisons of calculated spectra with data are displayed for the incident energies $E_{\rm in} = 14.1$ and 18 MeV in Figs. 4 and 5, respectively. The calculations at $E_{\rm in} = 14.1$ MeV are in good agreement with the data for $E_{\rm out} > 6.5$ MeV at $\theta_{\rm c.m.} = 30^\circ$, 60°, and 100° and for $E_{\rm out} > 10$ MeV at $\theta_{\rm c.m.} = 150^\circ$.

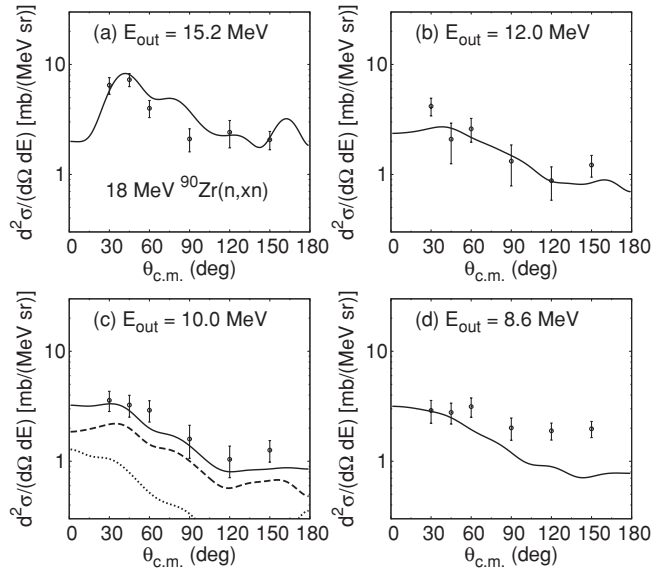

FIG. 7. (n,xn) angular distributions for 18-MeV neutrons incident on ^{90}Zr. Cross sections calculated with the CDM3Y3 interaction (full curves) are compared to experimental data [34] (open circles). The neutron outgoing energies $E_{\rm out}$ are indicated on panels (a), (b), (c), and (d). Dashed and dotted curves in panel (c) are for one-step calculations performed with only natural and only non-natural parity excitations, respectively.

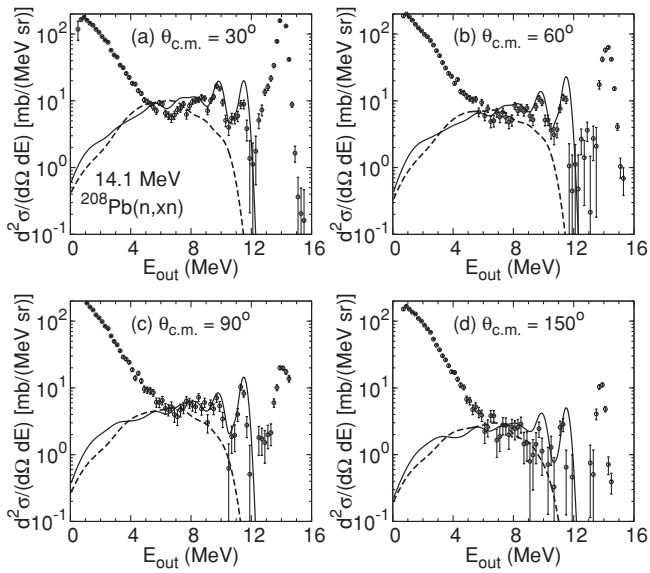

FIG. 8. Same as Fig. 4 for 14.1-MeV neutrons incident on ^{208}Pb. Data are from [35].

The discrepancy observed at $\theta_{\text{c.m.}} = 30^\circ$ for $E_F \simeq 12$ MeV is discussed later. For $E_{\text{in}} = 18$ MeV (see Fig. 5), good agreement is also found for $E_{\text{out}} > 8$ MeV at $\theta_{\text{c.m.}} = 30^\circ, 60^\circ$, and 90° and for $E_{\text{out}} > 10$ MeV at $\theta_{\text{c.m.}} = 150^\circ$. As expected, emission at low energy, and more particularly at large angles, is underestimated, as it should be dominated by the compound nucleus evaporation and most likely by the MSC process, both of which are not considered in the present analysis.

For $E_{\text{in}} = 14.1$ MeV in Fig. 4(a), the experimental neutron emission at $\theta_{\text{c.m.}} = 30^\circ$ and $E_{\text{out}} \simeq 12$ MeV is clearly underestimated. A possible explanation is that the first 2^+ state located at $E_{\text{exp}} = 2.186$ MeV in the experimental ^{90}Zr spectrum [23], which could provide a large contribution to the neutron emission at $E_{\text{out}} = E_{\text{in}} - E_{\text{exp}} = 11.9$ MeV, is not taken into account in our calculation as such a low-lying 2^+ excitation is not predicted by the present RPA structure model (see Sec. II B). The same $E_{\text{in}} = 14.1$ MeV data were analyzed in [6], where the contribution of this 2^+ state to the neutron emission was taken into account using a collective phenomenological model. While this 2^+ level provided an important contribution, its excitation was not sufficient to fully explain the emission observed at $E_{\text{out}} \simeq 12$ MeV. Furthermore, the broadening of the elastic peak is quite large, and the discrepancy between data and calculations almost disappears at $E_{\text{in}} = 18$ MeV [see Fig. 5(a)]. Further work is thus required to establish the genuine origin of the observed underestimation.

Angular distributions are displayed in Figs. 6 and 7 for $E_{\text{in}} = 14.1$ and 18 MeV, respectively. Calculations are in global agreement with the data. However, the mismatch is seen between calculated angular distributions and experimental data for $\theta_{\text{c.m.}} > 45^\circ$ and $E_{\text{out}} = 8.6$ MeV, and for $E_{\text{in}} = 14.1$ and 18 MeV in Figs. 6(b) and 7(d), respectively. This could be easily explained by evaporation and MSC contributions that are not included in our calculations. Isotropic angular distribution components could be added to the present calculations to better reproduce the general trend observed in the data.

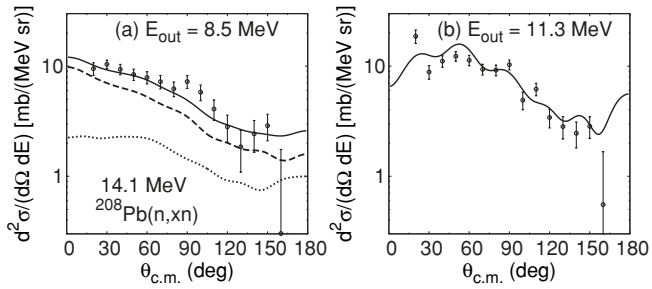

FIG. 9. Same as Fig. 7 for 14.1-MeV neutrons incident on ^{208}Pb. Data are from [35].

2. ^{208}*Pb target*

A similar analysis was performed for 14.1-MeV neutron scattering from ^{208}Pb. Comparisons between predictions and data for spectra and angular distributions are displayed in Figs. 8 and 9, respectively. The experimental cross sections are fairly well reproduced by our calculations. Note that the calculated one-step cross section for ^{208}Pb at 14.1 MeV is higher than that for ^{90}Zr, as seen in Fig. 4 for the same incident energy. This difference occurs not only because of the higher level density but also because of the stronger collectivity present in the ^{208}Pb excited states. A good illustration is the angular distribution at $E_{\text{out}} = 8.5$–8.6 MeV, which needs a multistep compound and/or evaporation components in the ^{90}Zr case [see Fig. 6(b)], while the one-step direct cross section still dominates the distribution for ^{208}Pb, as seen in Fig. 9(a).

3. *Reaction cross sections*

Ratios of the total one-step direct process contribution to the reaction cross section (σ_R) are provided in Table I for ^{90}Zr and ^{208}Pb at three different incident neutron energies, namely, 10, 14.1, and 18 MeV. The σ_R values have been obtained using the Koning-Delaroche optical potential [32]. The total cross section for the one-step process $\sigma^{(1)}$ corresponds to the double- differential cross section [Eq. (4)] integrated over outgoing angles and energies. The $\sigma^{(1)}$ values have been calculated with the CDM3Y3 interaction. As seen in Table I, the ratio $\sigma^{(1)}/\sigma_R$ increases with increasing incident energies and reaches 21% and 33% at $E_{\text{in}} = 18$ MeV for ^{90}Zr and ^{208}Pb, respectively. This ratio is stronger in ^{208}Pb, as the level density and collectivity content are higher than in ^{90}Zr.

TABLE I. Reaction cross sections σ_R and ratios of the total one-step cross section $\sigma^{(1)}$ to σ_R for neutron scattering off ^{90}Zr and ^{208}Pb at 10-, 14-, and 18-MeV incident energies.

	E_{in} (MeV)	σ_R (b)	$\sigma^{(1)}/\sigma_R$ (%)
	10	1.819	10.45
^{90}Zr	14.1	1.743	15.90
	18	1.707	20.70
	10	2.545	21.85
^{208}Pb	14.1	2.527	26.65
	18	2.498	32.87

C. RPA versus particle-hole excitations

The cross sections calculated with the RPA description of the excited states [Eq. (7)] are next compared to those obtained with p-h excitations [Eq. (11)] in Figs. 4 and 5 for ^{90}Zr and in Fig. 8 for ^{208}Pb.

In general, cross sections calculated with p-h excitations (dashed curves) are significantly lower than those obtained with the RPA excitations (full curves) and underestimate data at high emission energy. These differences can be directly related to those observed between p-h and RPA $B(EJ)$ values, discussed in Sec. II C for the E3 and E5 transitions. The relation between the magnitude of the cross section and $B(EJ)$ value can be understood by taking as an example the simple collective model for inelastic scattering [6,36]. In this model, differential cross sections are directly proportional to the square of the deformation parameter β_L [6] for any natural parity transition ($J = L$). In that case, the quantity β_L^2 can be simply related to the reduced transition probabilities $B(EJ)$ in Eq. (10) for the electric multipole [36], and DWBA inelastic-scattering cross sections thus exactly scale as $B(EJ)$ values. While in the present paper inelastic cross sections are obtained using the microscopic approach depicted in Sec. II A, which requires using the full transition density matrices [16], we can assume that the magnitude of the calculated cross section roughly scales as the associated $B(EJ)$ value.

Changes between p-h– and RPA-based cross sections in Figs. 4, 5, and 8 qualitatively follow those for the E3 and E5 reduced transition probabilities displayed in Figs. 1 and 2. However, cross-section variations are not exactly similar to variations of E3 and E5 strengths, as excitations with other multipolarities contribute significantly, as discussed in the next section. This comparison provides a measure of the impact of collectivity content of excited states on scattering properties and illustrates how a good description of this collectivity, provided by an accurate well-established nuclear-structure model, is of key importance to performing reliable calculations of direct pre-equilibrium emission cross sections.

However, the relation between the magnitude of DWBA cross sections and $B(EJ)$ values does not hold for (i) non-natural parity transitions, which would require an analysis of other spectroscopic quantities such as magnetic transition probabilities $B(MJ)$, and (ii) isovector transitions. But as for excitation energies below 15 MeV, which are relevant for the present study, the isoscalar transitions to natural parity states provide the main contributions to the one-step cross section, their analysis is sufficient to understand the impact of collectivity on calculated spectra. An exception is the IVGDR, which is mainly isovector in nature, but in the present analysis conducted below 20 MeV the transition to this state does not provide a large contribution to the one-step cross sections (see Sec. III D).

D. Spin and parity components

Our model analysis focuses next on the spin and parity content of transitions feeding excited states. For convenience a distinction is made between natural [$\Pi = (-)^J$] and non-natural [$\Pi = (-)^{J+1}$] parity transitions.

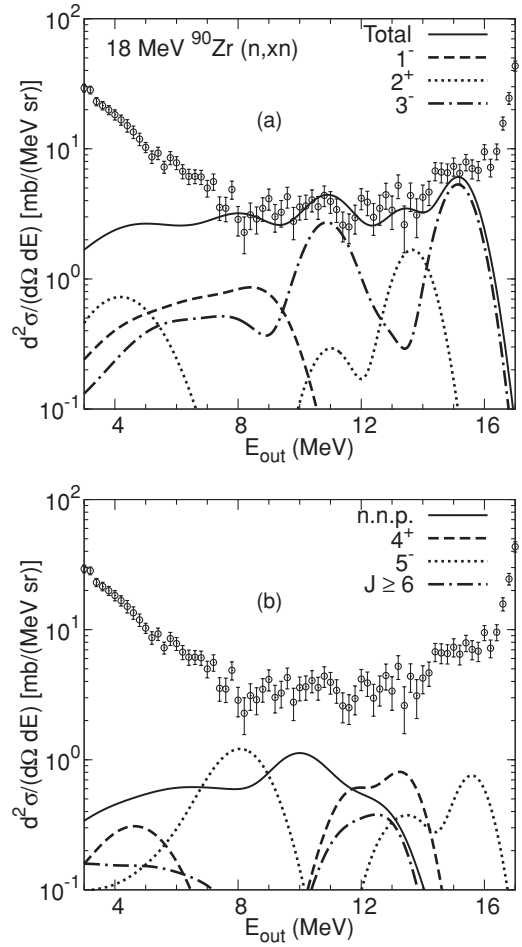

FIG. 10. The 18-MeV neutrons incident on ^{90}Zr. Contributions of the different spin-parity J^Π transitions to the one-step cross section for the neutron emission at $\theta_{\text{c.m.}} = 30^\circ$ and at E_{out} in the range 3–17 MeV. Circles are for experimental data. In panel (a), full, dashed, dotted, and dot-dashed curves are for calculations using excitations with all multipolarities (total), $J^\Pi = 1^-$, $J^\Pi = 2^+$, and $J^\Pi = 3^-$, respectively. In panel (b), full, dashed, dotted, and dot-dashed curves are for calculations using excitations with non-natural parity (n.n.p.), $J^\Pi = 4^+$, $J^\Pi = 5^-$, and natural parity and $J \geqslant 6$, respectively.

Spectra tied with natural parity transitions are discussed at first place for $\theta_{\text{c.m.}} = 30^\circ$ in the interaction between 18- and 14.1-MeV neutrons incident on ^{90}Zr (Fig. 10) and ^{208}Pb (Fig. 11), respectively. Inelastic scattering cross sections for ground-state to excited-state transitions, where J grows from $J = 1$ to $J = 3$, are shown as dashed, dot, and dot-dashed curves, respectively, in Figs. 10(a) and 11(a). Similar analyses are shown in Figs. 10(b) and 11(b), where the dashed, dot, and dot-dashed curves are for $J = 4$, $J = 5$, and $J \geqslant 6$, respectively. The full curves in Figs. 10(a) and 11(a) are for the total one-step emission, that is, with $J = 0$–14, and $\Pi = +$ and $\Pi = -$.

As can be seen in Fig. 10(a) for ^{90}Zr, the 3^- excitations (dot-dashed curve) provide the main contribution to the one-step process. These excitations are responsible for the high-emission-energy peak and most of the spectrum emission at $E_{\text{out}} \sim 11$ MeV, that is, for the LEOR energy

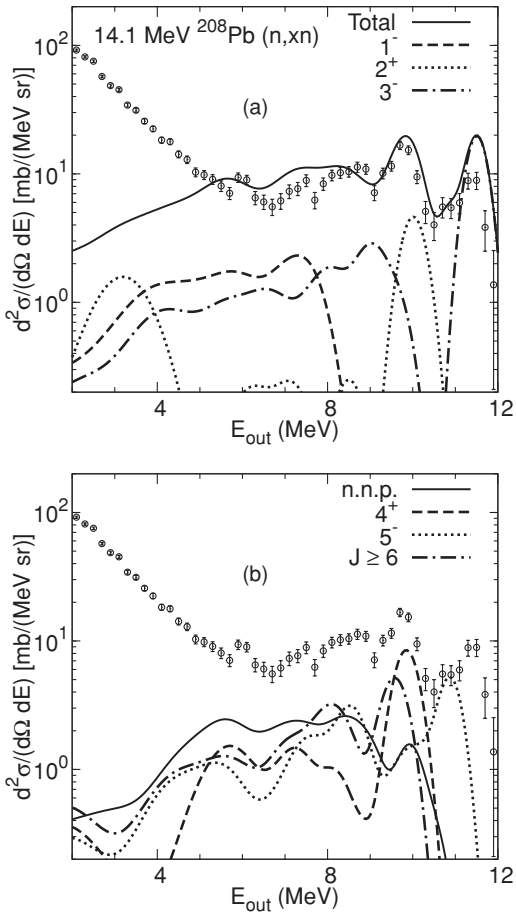

FIG. 11. Same as in Fig. 10 for 14.1-MeV incident neutrons on ^{208}Pb and for $E_{\rm out}$ in the range 2–12 MeV.

($E_x \sim 6.9$ MeV). Another key contribution to the spectrum, which originates from the 2^+ level excitations, displays a maximum for $E_{\rm out} \sim 13.5$ MeV. Transitions with higher multipolarities (i.e., with $J > 3$) also contribute significantly to neutron emission, as shown in Fig. 10(b). A quite strong $J^\Pi = 5^-$ component is observed for the outgoing energy $E_{\rm out} \sim 8$ MeV, stemming from collective transitions predicted in SCRPA+D1S calculations at an excitation energy near $E_x \sim 9.8$ MeV.

The multipolarity decomposition of the spectra is next extended to the 14.1-MeV data shown in Figs. 11(a) and 11(b) for the ^{208}Pb target. At $E_{\rm out} \gtrsim 9$ MeV, the cross-section components arising from excitation of low-lying 2^+ and 3^- states [Fig. 11(a)] and from 4^+, 5^-, and 6^+ levels [Fig. 11(b)] add up to form broad peaks shown as solid curves. At lower outgoing energies, all depicted spin and parity contributions are required to describe neutron emission. We notice that the $J \geqslant 6$ component is quite strong, as shown as the dot-dashed curve in Fig. 11(b). This arises from $J \geqslant 6$ collective strength, especially that for $J^\Pi = 6^+$ excitations below $E_x \sim 7$ MeV (details not shown).

Excitation of giant resonances also contributes to the calculated spectra. For example, contributions from ISGQR excitations are shown as dotted curves with maxima at $E_{\rm out} \simeq 4$ MeV in Fig. 10(a) and at $E_{\rm out} \simeq 3$ MeV in Fig. 11(a). For both targets, the components arising from the ISGQR and IVGDR excitations are too weak to be seen in the present spectra, as they both are calculated at $E_x \sim 13.5$ MeV (^{208}Pb) and $E_x \sim 17.8$ MeV (^{90}Zr). At incident energies as low as 14.1 and 18 MeV, their excitation is small as compared to compound nuclear emission. However, ISGQR and IVGDR excitations will become of key importance in the interpretation of spectra measured at higher incident energies.

The contribution of the non-natural parity transitions to the calculated spectrum is shown as a full curve in Fig. 10(b) for 18-MeV neutrons incident on ^{90}Zr, where this component amounts to approximately 30% of the total one-step emission for $E_{\rm out} \lesssim 13$ MeV, that is, for $E_x \gtrsim 5$ MeV. Another example of non-natural parity transition contributions to differential spectra at $E_{\rm out} = 10$ MeV is shown as a dotted curve in Fig. 7(c). The dashed curve is for natural-parity transitions. This latter component is 30% smaller than the angular distribution for the full emission spectrum (full curve). The same analysis for ^{208}Pb leads to similar conclusions, as suggested considering the spectrum in Fig. 11(b) and the angular distribution in Fig. 9. These specific examples illustrate in a quantitative way the typical portion of the emission spectra originating from non-natural parity excitations. Their relative amount remains stable, with outgoing energies corresponding to $E_x = E_{\rm in} - E_{\rm out}$, with $E_x \gtrsim 5$ MeV for both targets.

E. Consistent treatment of p-h and collective excitations

We now provide a detailed discussion of the approximations adopted in the previous MSD model implementations [5–7], which we contrast to the present model approach.

Analyses of the 14- and 18-MeV neutron-induced reactions on ^{90}Zr and ^{208}Pb were performed previously in [5–7]. In these works it was assumed that direct reactions can proceed following two distinct mechanisms, namely, inelastic scattering to discrete collective states and direct pre-equilibrium emission. Collective discrete cross sections for isoscalar natural parity transitions were calculated within the macroscopic collective model using deformation parameters β_L deduced from proton inelastic-scattering data analyses. These discrete contributions were then incoherently added to the pre-equilibrium component, calculated within the MSD model implemented with incoherent p-h excitations [5,6], or within the exciton model [7].

Applying this procedure raises two main concerns. First, an accurate calculation of the direct cross section with the macroscopic collective model relies on a very precise knowledge of the β_L values for all collective excitations of levels lower than incident energies. This requirement can hardly be fulfilled in general, as many collective states above the first few low-lying states that significantly contribute to emission spectra are not experimentally well known, even for closed- and near-closed-shell nuclei. Phenomenological procedures have been used so far to take into account this collectivity for multipoles $L \leqslant 4$, and possible collective contributions for higher multipoles have not been considered. For instance, the LEOR contribution has been included in [5–7], considering a β_L value based on an assumed fraction of the EWSR, the amount of which greatly varies between the different analyses.

In [6], collectivity at excitation energy above a few MeV for multipoles other than $L = 3$ is neglected. In the works of [7,9], collective contributions with multipoles up to $L = 4$ are considered using an approximate procedure to fully exhaust the EWSRs, but these are neglected for $L > 4$ transitions.

A second concern is that the incoherent sum of direct collective and MSD cross sections can lead to double counting for the collective and incoherent p-h excitations. This problem has been handled through different phenomenological procedures. In Ref. [5], the pre-equilibrium contribution was gradually introduced from excitation energies above which collective contributions were assumed to vanish. Double counting was more precisely analyzed in [9], where the EWSR corresponding to both collective and incoherent p-h excitations was calculated for each multipole L and was shown to exceed the EWSR limit for transitions with $L \leqslant 4$. Double counting was then prevented, assuming that (i) for $L \leqslant 4$ transitions, contributions to the direct emission process are exclusively attributed to collective excitations, with corresponding EWSRs within theoretical bounds, and (ii) for $L > 4$, collectivity is small and smeared out enough so the direct emission can be calculated with the MSD model using incoherent p-h excitations.

The present microscopic reaction model overcomes these deficiencies by construction. First, it consistently describes the so-called collective direct and the one-step contributions to neutron emission. As a consequence, double counting is not an issue, as all the target states excited in the one-step mechanism are described within a unique structure model that properly exhausts the EWSRs [15]. Moreover, the SCRPA+D1S model ensures that the collectivity content of the target spectrum is accurately accounted for in the one-step cross section. For instance, the sums of the predicted fractions of the $J^{\Pi} = 3^-$ EWSR for low-lying states and the LEOR are 34% and 36% for ^{90}Zr and ^{208}Pb, respectively, values that are in good agreement with estimates based on previous Hadron scattering data analyses [37,38]. Finally, quite large collectivity for multipoles as high as $L = 6$ is also predicted by the SCRPA+D1S model, as discussed in Secs. III C and III D, and their contributions to the neutron emission are automatically included here as well.

F. Model uncertainties

Our calculations with no adjustable parameter are in good overall agreement with experimental data. We consider that an uncertainty of the order of 30% can be associated with normalization of the calculated cross section due to limited knowledge of the residual two-body interaction. However, different approximations used in our model may further increase this uncertainty.

First, we used the ansatz of local optical potential to generate the distorted waves, but it was demonstrated [39] that compared to the result obtained with a nonlocal optical potential, an equivalent local potential increases the probability amplitude of the distorted wave inside the nucleus (Perey effect). This leads to overestimation of the probability transition amplitudes of Eq. (3). Nonlocality corrections were introduced [39] to correct for this effect and used in MSD pre-equilibrium calculations [40]. As a result, one-step cross sections decreased by 35%. Here the phenomenological optical potential used in our calculations is energy dependent, which partly accounts for nonlocal properties. For this reason, and considering that the nonlocal potential to which the phenomenological local potential should be equivalent remains unknown, any estimation of the genuine nonlocality corrections becomes uncertain. Consequently, this correction was not included in our calculation, but it could significantly affect the normalization of the calculated cross sections.

Another source of uncertainty is tied with the many-body description of the target excitations. While the RPA method provides a good representation of both coherent (collective) and incoherent p-h excitations, it is not appropriate for the description of excitations with more complicated structure. A nuclear structure model that explicitly treats couplings to two or more p-h components and continuum states should be used, as these couplings will change the spectroscopic properties of the target excitations, and thus the associated inelastic cross sections, beyond the simple spreading and shifting described in Sec. II B and used in the present calculation. Pairing correlations, which are neglected in the HF and RPA approaches, should also be taken into account for single-closed-shell nuclei, as they would most likely impact both excitation energies and strength functions. Including pairing in the description could improve the description of low-lying positive parity states in ^{90}Zr and thus the predictions for associated pre-equilibrium emission at high energy.

Finally, other components of pre-equilibrium emission, namely, the two-step direct and the multistep compound processes, may have some contributions even at emission energies where the one-step process seems to dominate. Although we believe their impact on the current analysis could be small, these contributions should be considered to better assess the quality of our one-step calculation during comparison with data. However, as these components have so far been calculated only with phenomenological ingredients and adjusted together with the one-step direct component to match experimental cross sections, their exact individual contributions to the pre-equilibrium emission remain difficult to assess.

IV. CONCLUSION AND OUTLOOK

We have performed quantum-mechanical calculation of the one-step direct component of the pre-equilibrium (n, n') emission using an effective two-body residual interaction and a microscopic description of the target states based on RPA calculations implemented with the D1S force. Density-dependent M3Y forces have been considered for the residual two-body interaction between projectile and target nucleons. Our reaction model does not contain any adjustable parameters, and the calculated cross sections have been directly compared to the data. For a 14- and 18-MeV neutron-induced reaction on ^{90}Zr and ^{208}Pb targets, the predicted neutron spectra and angular distributions are in overall good agreement with the data.

The collective content of the target spectra described within the RPA approach is shown to be appropriate to correctly describe the measured neutron emission. Calculations performed with incoherent particle-hole excitations, which neglect collectivity, underestimate the data at high emission energy. The present one-step calculation automatically accounts for contributions of collective and noncollective states, giant resonances, and non-natural parity excitations. Consequently, our model does not consider any arbitrary distinction between the pre-equilibrium one-step process and direct excitation of collective states. This removes some modeling ambiguities present in previous more phenomenological analyses, such as (i) double counting between collective states and incoherent p-h excitations, and (ii) incomplete and/or inaccurate evaluation of the collective states' contributions to the neutron emission. Our model also shows that collective transitions with multipolarity as high as $L = 5$ (^{90}Zr) and $L = 6$ (^{208}Pb) are required to fully account for calculated spectra. It was also found that non-natural parity excitations contribute up to 30% of the double-differential one-step cross section.

We have discussed uncertainties inherent to our model prescription, namely, those tied with residual interactions. This discussion is far from being closed, as we are still using phenomenological potentials in the incoming and outgoing reaction channels.

These concerns could be alleviated if one considers microscopic one-step calculations for proton-induced reactions at higher energy ($E > 50$ MeV), since microscopic nonlocal optical potentials can be built [12,27], and the effective two-body force to be used as a residual interaction is more precisely known [27]. Calculated spectra at incident energies higher than 20 MeV will reveal the growing importance of exciting giant resonances that lie in the spectra of targets between approximately 10 and 40 MeV. These excitations are expected to significantly contribute to the direct pre-equilibrium emission in this energy regime.

The present study will be extended in the near future to spherical open-shell nuclei using the self-consistent quasiparticle RPA (QRPA) nuclear-structure approach implemented with the Gogny force [41]. The impact of collectivity predicted by this QRPA model on pre-equilibrium cross sections will also be studied for open-shell nuclei such as ^{238}U [42,43].

ACKNOWLEDGMENTS

One of the authors (M.D.) is very grateful to D. Gogny for his advice and guidance throughout the early stage of this work performed at CEA-DAM Ile-de-France. He is also very grateful to J. Raynal for his continuous assistance with the DWBA98 code. He also wishes to thank S. Péru for helpful guidance with the RPA formalism and computer code. This work was supported in part by the UNEDF SciDAC Collaboration and was partly carried out under the auspices of the National Nuclear Security Administration of the US Department of Energy at Los Alamos National Laboratory under Contract No. DE-AC52-06NA25396.

[1] H. Feshbach, A. Kerman, and S. Koonin, Ann. Phys. (NY) **125**, 429 (1980).
[2] M. B. Chadwick and P. G. Young, Phys. Rev. C **47**, 2255 (1993).
[3] M. B. Chadwick, P. G. Young, D. C. George, and Y. Watanabe, Phys. Rev. C **50**, 996 (1994).
[4] T. Kawano and S. Yoshida, Phys. Rev. C **64**, 024603 (2001).
[5] A. J. Koning and M. B. Chadwick, Phys. Rev. C **56**, 970 (1997).
[6] P. Demetriou, A. Marcinkowski, and P. E. Hodgson, Nucl. Phys. A **596**, 67 (1996).
[7] A. J. Koning and M. C. Duijvestijn, Nucl. Phys. A **744**, 15 (2004).
[8] A. J. Koning and J. M. Akkermans, Ann. Phys. (NY) **208**, 216 (1991).
[9] A. Marcinkowski and B. Marianski, Nucl. Phys. A **653**, 3 (1999).
[10] T. Tamura, T. Udagawa, and H. Lenske, Phys. Rev. C **26**, 379 (1982).
[11] J. F. Berger, M. Girod, and D. Gogny, Comput. Phys. Commun. **63**, 365 (1991), and references therein.
[12] M. Dupuis, S. Karataglidis, E. Bauge, J.-P. Delaroche, and D. Gogny, Phys. Rev. C **73**, 014605 (2006).
[13] J. P. Blaizot, D. Gogny, and B. Grammaticos, Nucl. Phys. A **265**, 315 (1976).
[14] J. P. Blaizot and D. Gogny, Nucl. Phys. A **284**, 429 (1977).
[15] J. Dechargé and L. Šips, Nucl. Phys. A **407**, 1 (1983).
[16] M. Dupuis, S. Karataglidis, E. Bauge, J.-P. Delaroche, and D. Gogny, Phys. Lett. B **665**, 152 (2008).
[17] J. Dechargé, L. Šips, and D. Gogny, Phys. Lett. B **98**, 229 (1981).
[18] J. Heisenberg, J. Dawson, T. Milliman, O. Schwentker, J. Lichtenstadt, C. N. Papanicolas, J. Wise, J. S. McCarthy, N. Hintz, and H. P. Blok, Phys. Rev. C **29**, 97 (1984).
[19] G. F. Bertsch, P. F. Bortignon, and R. A. Broglia, Rev. Mod. Phys. **55**, 287 (1983).
[20] D. Gambacurta, M. Grasso, and F. Catara, Phys. Rev. C **81**, 054312 (2010).
[21] M. Harakeh and A. van der Woude, *Giant Resonances* (Oxford University Press, New York, 2001).
[22] M. Martin, Nucl. Data Sheets **108**, 1583 (2007).
[23] L. Ekström and J. Lyttkens-Linden, Nucl. Data Sheets **67**, 579 (1992).
[24] J. Raynal, computer code DWBA98, 1998 (NEA 1209/05).
[25] J. Raynal, Nucl. Phys. A **97**, 572 (1967).
[26] M. Dupuis, Ph.D. thesis, Universtité de Bordeaux I, 2006.
[27] K. Amos, P. J. Dortmans, H. V. von Geramb, S. Karataglidis, and J. Raynal, Adv. Nucl. Phys. **25**, 275 (2000).
[28] K. Amos, S. Karataglidis, and Y. J. Kim, Nucl. Phys. A **762**, 230 (2005).
[29] D. T. Khoa, G. R. Satchler, and W. von Oertzen, Phys. Rev. C **56**, 954 (1997).
[30] N. Anantaraman, H. Toki, and G. F. Bertsch, Nucl. Phys. A **398**, 269 (1983).
[31] D. T. Khoa and W. von Oertzen, Phys. Lett. B **304**, 8 (1993).
[32] A. J. Koning and J.-P. Delaroche, Nucl. Phys. A **713**, 231 (2003).
[33] A. M. Kobos, B. A. Brown, P. E. Hodgson, G. R. Satchler, and A. Budzanowski, Nucl. Phys. A **384**, 65 (1982).
[34] M. Baba, M. Ishikawa, N. Yabuta, T. Kikuchi, H. Wakabayashi, and N. Hirakawa, in *Proceedings of the International Conference on Nuclear Data for Science and Technology*, edited by S. Igarasi (Saikon Publishing, Tokyo, 1988), p. 1185.

[35] A. Takahashi, J. Yamamoto, K. Oshima, M. Ueda, M. Fukazawa, Y. Yanagi, J. Miyagachi, and K. Sumita, J. Nucl. Sci. Technol. **21**, 577 (1984).
[36] G. R. Satchler, *Direct Nuclear Reactions* (Oxford University Press, New York, 1983).
[37] Y. Fujita, M. Fujiwara, S. Morinobu, I. Katayama, T. Yamazaki, T. Itahashi, H. Ikegami, and S. I. Hayakawa, Phys. Rev. C **32**, 425 (1985).
[38] Y. Fujita, T. Shimoda, H. Miyatake, N. Takahashi, M. Fujiwara, S. Morinobu, T. Yamagata, J. Takamatsu, A. Terakawa, and H. Folger, Phys. Rev. C **45**, 993 (1992).
[39] F. Perey and B. Buck, Nucl. Phys. **32**, 353 (1962).
[40] Y. Watanabe *et al.*, Phys. Rev. C **51**, 1891 (1995).
[41] S. Péru and H. Goutte, Phys. Rev. C **77**, 044313 (2008).
[42] M. Dupuis, E. Bauge, L. Bonneau, J.-P. Delaroche, T. Kawano, S. Karataglidis, and S. Péru, in *Proceedings of the Second International Workshop on Nuclear Compound Reactions and Related Topics*, edited by L. Bonneau, N. Dubray, F. Gunsing, and B. Jurado (EPJ Web of Conferences, vol. 2, Les Ulis, 2010), p. 11001.
[43] S. Péru, G. Gosselin, M. Martini, M. Dupuis, and S. Hilaire, Phys. Rev. C (to be published).